Available online at www.sciencedirect.com
SCIENCE DIRECT®
Mechanics of Materials 35 (2003) 1107–1126
MECHANICS OF MATERIALS
www.elsevier.com/locate/mechmat

Supercritical matrix microcracking in brittle matrix plain weave composites under uniaxial tension

S.I. Haan [a], P.G. Charalambides [a,*], J.L. Kuhn [b], M.C.L. Patterson [c]

[a] *Department of Mechanical Engineering, The University of Maryland Baltimore County, 1000 Hilltop Circle, Baltimore, MD 21250, USA*
[b] *Bldg 5 Rm C310A, NASA/GSFC Code 542, Greenbelt, MD 20771, USA*
[c] *Ceramic Composites Inc., 110 Benfield Blvd., Millersville, MD 21108, USA*

Received 15 June 2002; received in revised form 1 November 2002

Abstract

A stress induced supercritical non-linear microcracking model is employed as part of an incremental and iterative hierarchical modeling scheme aimed at investigating the evolution of damage in brittle matrix plain weave fabric composites subjected to uniaxial tension. The study focuses exclusively on matrix micro-damage and its effect on the macroscopic non-linear composite response. For a given load increment, the requisite micro-stresses and associated state of matrix microcracking are updated through an iterative converging scheme that employs the semi-analytical approximate model to compute micro-stresses and the discrete microcracking model to evaluate micro-damages. A wide range of non-linear stress–strain curves were obtained through parametric studies. Degradation of the in-plane effective properties of the unit-cell and evolution of the volumetric matrix damage were monitored throughout the simulations. The simulated predictions were then used to develop empirical in-plane effective property degradation laws in terms of the applied loading. Damage-induced macroscopic elastic anisotropies were predicted as was the formation of macroscopic damage zones consistent with discrete micro-fracture events such as inter-bundle matrix cracking, bundle mode-I cracking, and transverse bundle matrix cracking. Stress–strain curves obtained from the model were compared favorably with their experimental counterparts obtained from literature and commercial sources.

Keywords: Ceramic; Woven; Composites; Microcracking; Damage; Non-linear; Stress-induced; Degradation

1. Introduction

This work which builds on previous research (Kuhn and Charalambides, 1998a,b, 1999; Kuhn et al., 1999, 2000) aims at investigating the effects of microcrack formation (Fu and Evans, 1985; Charalambides and McMeeking, 1987) and matrix damage evolution on the non-linear response of a plain weave ceramic matrix composite (CMC). In contrast to the previous work (Kuhn et al., 2000), in this study, supercritical stress-induced microcracking conditions are employed in the non-linear damage evolution model development. The concept of supercriticality in microcracking is somewhat analogous to the same concept employed in

* Corresponding author. Tel.: +1-410-455-3346/3313; fax: +1-410-455-1052.
E-mail address: panos@umbc.edu (P.G. Charalambides).

0167-6636/$ - see front matter © 2003 Elsevier Ltd. All rights reserved.
doi:10.1016/S0167-6636(03)00006-1

modeling phase transformation of particle reinforced ceramic composites such as zirconia toughened alumina (Lambropoulos, 1988), wherein zirconia particles are assumed to transform *completely* from a tetragonal phase to a monoclinic phase when subjected to a critical hydrostatic pressure.

Supercritical microcracking employed herein, models a similar behavior in which at a critical stress level material points in the continuum are assumed to exhaust their microcracking potential and thus, are assigned the maximum allowed microcrack density which is often referred to as the saturation microcrack density denoted by ϵ_s. Unlike the subcritical microcracking case addressed in the work by Kuhn et al. (2000), wherein appreciable transient microcrack zones are predicted between the zero-damage zone and the saturated zone, in this supercritical case, the transient zone would be non-existent giving rise to abrupt changes in the state of damage along the boundaries of the microcrack damage zone. To a certain extent, this condition may be more representative of the cracking processes observed in CMCs wherein *regularly* spaced bridged and unbridged matrix cracks are common types of micro-failure.

Like the subcritical microcracking study presented in the work by Kuhn et al. (2000), the focus of this work is also on the matrix damage evolution and its effects on the non-linear response of a plain weave CMC. Thermal stress effects induced by constituent thermal expansion mismatch are not considered. Thus, simulations and comparisons to experiments reported in this study are restricted to a SiC/SiC system for which thermal stresses are negligible as reported by Wang and Singh (1994). A detailed presentation of the model development can be found in the work by Kuhn et al. (2000). For a brevity purpose, we shall proceed to present only a short summary of the general modeling scheme, while presenting the supercritical microcracking aspect of the model in greater detail.

2. General modeling approach

The non-linear supercritical microcracking damage model presented in this work is comprised of the linear model predicting the elastic microfields in the woven unit-cell and the microcracking model to compute and update the status of microcracking damage in the system. Detailed descriptions of the sub-models employed in the integrated linear model as well as more thorough accounting of the subcritical microcracking model are presented in the work by Kuhn et al. (2000). Thus, the linear part of the model will be briefly reviewed earlier in the section and then, the supercritical microcracking condition will be addressed in greater detail.

2.1. Linear elastic woven unit-cell micro-fields

The model employed the woven unit-cell geometry developed by Kuhn and Charalambides (1999), which was inspired by a few pioneering works of Ishikawa and Chou (1982a,b, 1983a,b) and Whitcomb (1991). In this geometry model, the woven composite is treated as a composite laminate with four non-uniform layers. Extensive discussion on each of the geometry features and the detailed presentation of the surface functions used to represent the top and bottom surface of each layer can be found in the work by Kuhn and Charalambides (1999). The woven unit-cell is comprised of the warp tows, the fill tows, and the inter-bundle matrix phases at the mesoscopic scale as shown in Fig. 1a. A rigorous hierarchical micro-mechanics model utilizing the Hashin composite cylinder assemblage model (see Hashin, 1983) and the porous solid model employed by Bassani (1991), used for bundle homogenization is fully presented in the work by Kuhn and Charalambides (1998a). The boundary value problem under consideration is that associated with uniaxial tension in the x-direction. The remotely applied uniaxial loading F_x^{∞} on a woven ply is simulated with the displacement boundary conditions applied to the symmetric woven unit-cell using appropriate symmetry conditions as discussed by Kuhn et al. (1999). The unit-cell geometry, material properties, and boundary conditions outlined above constitute an elasticity boundary value problem in three-dimensions. The problem is reduced to a two-dimensional plate

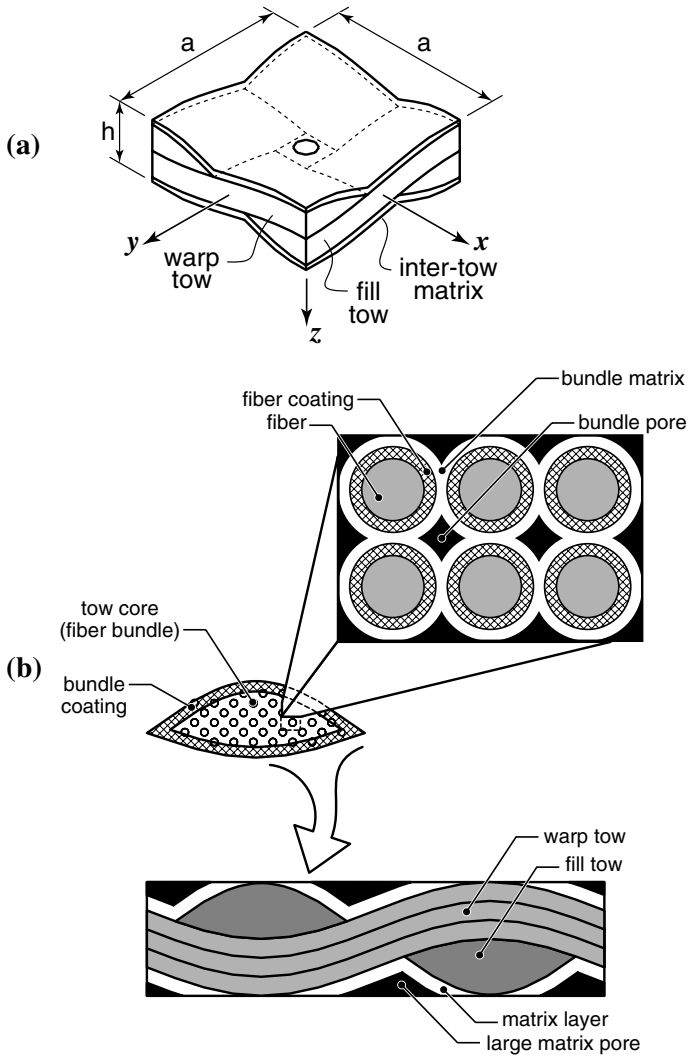

Fig. 1. (a) The woven unit-cell comprised of four mesoscopic phases: the lower matrix, the fill tow, the warp tow, and the upper matrix. (b) Hierarchical schematics presenting a typical microstructure of CVI ceramic matrix plain weave composite.

elasticity boundary value problem by employing the Kirchhoff–Love deformation hypothesis and its approximate analytical solutions are obtained by the Rayleigh–Ritz method, which is comprehensively discussed by Kuhn et al. (1999). The above semi-analytical model has been shown to yield sufficiently accurate predictions on the elastic micro-strain and micro-stress fields experienced by woven micro-constituents due to general in-plane loading (Kuhn et al., 1999).

2.2. Stress induced matrix microcracking model

As mentioned earlier, the subcritical microcracking condition cannot be used to simulate or investigate microcracking mechanisms associated with an abrupt microcracking event. In order to expand the model capability to simulate the above phenomenon, the supercritical microcracking model is developed herein. As such, the supercritical condition model is complementary to

the subcritical microcracking model first developed by Charalambides and McMeeking (1987, 1988).

2.2.1. The supercritical microcracking continuum

The microcracking continuum model founded on the work of Fu and Evans (1985) employed herein, was developed by Charalambides and McMeeking (1987, 1988). The key idea of the model is that an effective stress measure such as that used by Charalambides and McMeeking (1987) can be used to update the microcrack density ϵ, as defined by Budiansky and O'Connell (1976), at every point in the solution domain. It is important to note that the microcracking model employed herein is used as a simple but effective tool to account for the material stiffness degradation due to microcracking damage at a point as a function of the associated stress state.

As will become evident later on, the study focuses primarily on assessing the damage-induced non-linear response of a woven CMC system and as such it employs a rather simple but effective stiffness degradation law for the microcracking continuum. At the same time, it is important to note that more sophisticated microcracking models such as those developed by Horii and Nemat-Nasser (1983a,b), Hoenig (1979, 1982), Hashin (1990, 1991, 1995), Ortiz and Giannakopoulos (1989), Giannakopoulos (1989, 1990), Krajcinovic and Fonseka (1981), Krajcinovic (1985), Hoagland et al. (1976), Hoagland and Embury (1980), and Voyiadjis (1995a,b) could also be implemented at later stages as needed to more realistically capture the damage-induced non-linear response of woven CMCs. The implementation of such models would be needed if, for example, microcrack surface closure effects, microcrack proximity effects, and pointwise microcrack induced elastic anisotropies were to be accounted. In light of the above, the proposed supercritical matrix microcracking model should be employed in instances wherein surface crack closure, local microcrack induced anisotropies, and even local microcrack dilatation effects as discussed by Charalambides and McMeeking (1987, 1988) are of secondary importance, when compared to the effects of material property degradation.

The implementation of the microcracking model and parametric studies presented in this work are performed through the independent model parameters such as the microcracking rate constant λ, the first microcracking critical stress σ_c, the saturation microcracking stress σ_m and saturation microcracking density ϵ_s.

The microcracking model is represented by a microcracking law which relates the current state of stress to the current state of microcracking damage. As discussed earlier, microcracking can occur, generally speaking, in two different ways. Under the "subcritical" condition, the material is damaged gradually before it is saturated. This condition, which was addressed in the work by Kuhn et al. (2000), is enforced by employing the microcracking law shown in Fig. 2a. It is important to note that under the subcritical microcracking condition, the material at a point of interest experiencing an equivalent stress between the first critical stress σ_c and the saturation stress σ_m is assigned microcrack densities on the rising branch of the microcracking law. Thus, damage saturation at a point is only allowed when the equivalent stress σ_e exceeds the saturation microcracking stress σ_m. Under this condition, the local stress–strain curve exhibits a smooth transition branch from the point of microcracking initiation to the saturation point as shown in Fig. 2b. Unlike the subcritical condition, the supercritical microcracking requires that once microcracking initiates at a point, the damage progresses instantly to its maximum saturation level ϵ_s consistent with the microcracking law shown in Fig. 2c. As a result, the associated stress–strain curve exhibits a discontinuous jump upon supercritical microcracking as shown in Fig. 2d.

Thus, in accordance with Fig. 2c, the discrete microcrack density ϵ under the supercritical condition is obtained in a form of step function as follows:

$$\epsilon = \begin{cases} 0 & \text{for } \sigma_e < \sigma_c \\ \epsilon_s & \text{for } \sigma_e \geqslant \sigma_c \end{cases} \tag{1}$$

where ϵ is the microcrack density as defined by Budiansky and O'Connell (1976), and $\sigma_e = \sqrt{\sigma_{ij}\sigma_{ij}}$ is an equivalent stress. The parameter σ_c represents the equivalent stress at which microcracking initi-

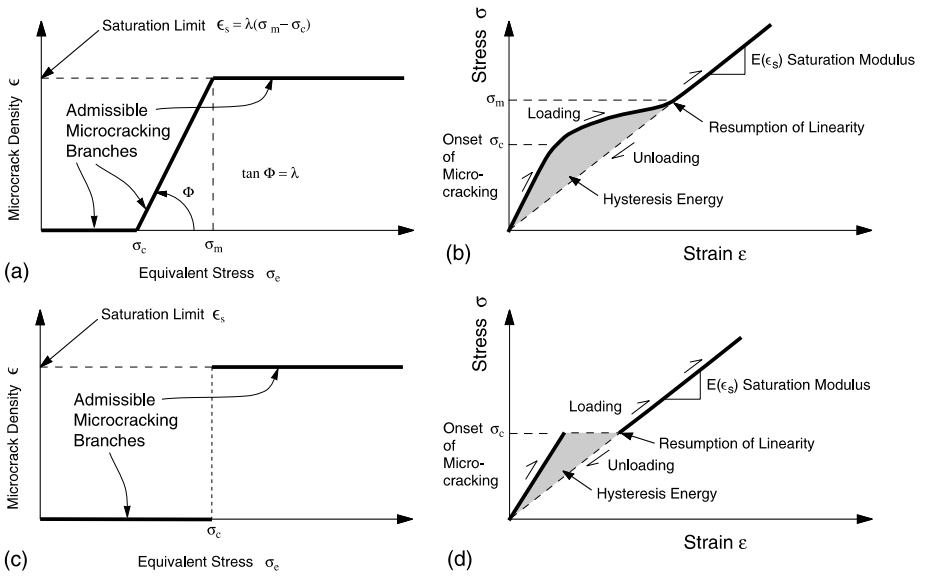

Fig. 2. (a) Subcritical microcracking law relating the microcrack density ϵ to the equivalent stress $\sigma_e (= \sqrt{\sigma_{ij}\sigma_{ij}})$. (b) The profile of the non-linear stress–strain curve of an isotropic microcracking continuum under subcritical condition. (c) The supercritical microcracking law. (d) The profile of the non-linear stress–strain curve of an isotropic microcracking continuum under supercritical condition.

ates. The saturation microcrack density is denoted by ϵ_s. Unlike the subcritical case presented in Fig. 2a showing the linearly increasing microcrack density, the microcrack density ϵ under the supercritical condition can be either 0 or equal to the saturation value ϵ_s. As discussed before, once the equivalent stress at the point of interest exceeds σ_c, the material at that point is damaged to its saturation microcrack density. Note that σ_c is equal to the saturation microcracking stress σ_m in the supercritical case. Charalambides and McMeeking (1988) approximated the Budiansky and O'Connell (1976) expressions for the effective elastic properties of a microcracking solid as follows:

$$\frac{\overline{E}}{E} = \frac{\bar{\nu}}{\nu} = 1 - \frac{16}{9}\epsilon = \frac{1}{f} \tag{2}$$

where $\overline{E}$ and $\bar{\nu}$ are the effective Young's modulus and Poisson's ratio of the microcracked solid, respectively and E and ν represent the properties of the undamaged solid. The microcracking parameter f is defined as an internal state variable for convenience. Consistent with Eq. (2), the stress–strain relationships for the microcracking solid take the form:

$$\sigma_{\alpha\beta} = \frac{E}{f + \nu^*}\left[\varepsilon_{\alpha\beta} + \frac{\nu^*}{f - \nu^*}\varepsilon_{\gamma\gamma}\delta_{\alpha\beta}\right] \quad \alpha, \beta, \gamma = 1, 2 \tag{3}$$

where $\nu^* = \nu$ for plane stress and $\nu^* = \nu/(1-\nu)$ for plane strain. In the above expression, repeated indices in a product imply summation over the index from 1 to 2. Also in Eq. (3), $\delta_{\alpha\beta}$ is the Kronecker delta in two-dimensions which takes the value of 1 when $\alpha = \beta$ or 0 when $\alpha \neq \beta$.

A schematic drawing of a uniaxial stress–strain curve that obeys Eq. (3) is shown in Fig. 2d. As shown, the material loads linearly without a loss of stiffness at all points wherein the effective stress σ_e is less than σ_c. Once exceeded, the microcrack density ϵ increases abruptly to ϵ_s, consistent with the microcracking law given in Eq. (1) and shown in Fig. 2c. Thus, upon the initiation of microcracking, ϵ becomes equal to ϵ_s which leads to material stiffness degradation consistent with Eq. (2). Thus, the horizontal branch of the stress–strain curve, shown in Fig. 2d, is clearly associated with the material loss of stiffness right at the moment when the effective stress at the point of interest σ_e reaches or exceeds the critical stress σ_c of

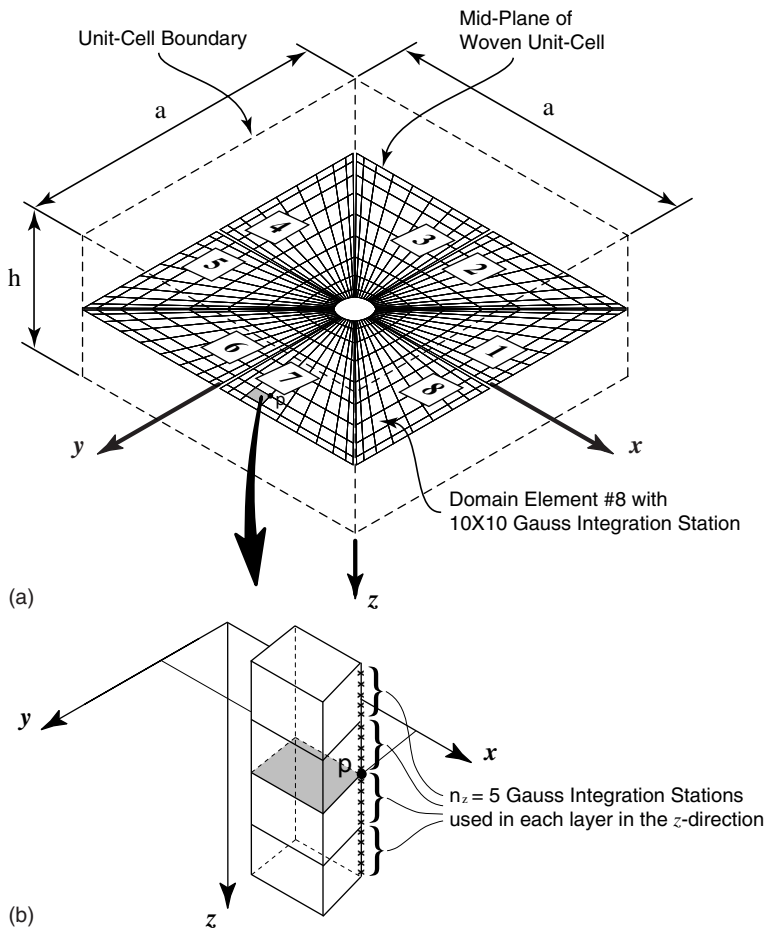

Fig. 3. (a) The x–y grid of Gauss integration stations used in the calculation of the volume integrals of the Rayleigh–Ritz method developed by Kuhn et al. (1999). (b) Integration in the out-of-plane z-direction is carried out using a user-controlled n_z number of Gauss points within each layer as shown above.

the microcracking continuum. Under both subcritical and supercritical microcracking conditions, upon unloading, the system unloads linearly along a path dictated by the degraded stiffnesses to zero stress for zero strain. Clearly, the adopted stress–strain law does not account for residual strains.

For a given state of strain at a point in the microcracking material under monotonically increasing loading, the microcrack density ϵ can be either 0 or the saturation microcrack density ϵ_s. Hence, f can have only two different values as shown below.

$$f = \begin{cases} 1 & \text{for } \epsilon = 0 \\ \left(1 - \frac{16}{9}\epsilon_s\right)^{-1} & \text{for } \epsilon = \epsilon_s \end{cases} \tag{4}$$

As the material is subjected to an arbitrary loading sequence, the microcrack density ϵ and damage parameter f may not decrease even as the material is unloaded. In the present case, the properties E and v represent the inter-bundle and bundle matrix properties E_m and v_m, respectively. Consequently, the degraded effective microcracked matrix properties are thus denoted as $\overline{E}_m$ and $\bar{v}_m$.

2.3. Non-linear response

In order to obtain the relationship between the applied strain $\hat{\varepsilon}^{\infty}$ and the resulting macroscopic stress $\hat{\sigma}^{\infty}$, a strain controlled secant incremental

and iterative scheme is employed. Initially the woven unit-cell is assumed to be unloaded with no residual stresses. In accordance with this assumption, the unit-cell is loaded incrementally by applying a remote strain $\hat{\varepsilon}^{\infty}$. At load increment i, a remote strain of $\hat{\varepsilon}_i^{\infty} = \hat{\varepsilon}_{i-1}^{\infty} + \Delta\hat{\varepsilon}_i^{\infty}$ with $\hat{\varepsilon}_0^{\infty} = 0$ is applied to the unit-cell. The reciprocal remote stress $\widehat{\sigma}_i^{\infty}$ is then computed with the aid of an iterative procedure. The first iteration ($j = 1$), is carried out using the degraded matrix properties obtained from the load step $i - 1$. This invariably leads to an overestimated stress $(\widehat{\sigma}_i^{\infty})^{j=1}$. The new stress $(\widehat{\sigma}_i^{\infty})^{j}$ and associated micro-stress fields are then used to update the microcracking parameter f_i^j at all integration points of the unit-cell. It is important to note that under the supercritical condition, the internal microcracking state variable f_i^j can assume values of 1.0 or the saturation level f_s, depending on the state of stresses at the point. The next iteration ($j = 2$) is then carried out using the degraded matrix properties obtained from the previous iteration. A loading step is finished only when consistent values for the internal state variable f are obtained for two consecutive iterations. The converged solution is then stored in association with the applied strain ε_i^{∞} and stress σ_i^{∞}. The new strain increment is then applied as needed to incrementally impose the specific magnitude of remote loading on the problem. At the end of the loading procedure, a library of damage data and effective properties associated with a specific level of remote load is obtained. This enables the study of both the progression of matrix micro-damage and the degradation of the unit-cell effective properties as a function of the applied load. More detailed presentation on this iterative scheme can be found in the work by Kuhn et al. (2000).

In the model implementation, the Gauss integration scheme is employed to compute the stiffness terms of the semi-analytical approximate model employed in obtaining the related micro-fields. Eight isoparametric domain elements as shown in Fig. 3a are introduced as needed to compute the high stress gradients in the vicinity of the pre-existing void as discussed elsewhere (Kuhn et al., 1999). Within each domain element, a user-controlled $M \times N$ Gauss integration stations are used consistent with the convergence studies of the semi-analytical approximate model reported by Kuhn et al. (1999). A user-controlled n_z Gauss integration stations are also introduced in the thickness z-direction as shown in Fig. 3b. As a result, a total of $8 \times M \times N \times n_z$ number of Gauss integration points are used to evaluate the stiffness terms of the semi-analytical approximate model and to update the state of damage.

3. Microcracking simulations

The simulations were carried out in a non-dimensional environment. The spatial variables are normalized by a characteristic length L_c which in this study is set to be equal to the unit-cell half period a. The shear and Young's moduli of each micro-constituent, mesoscopic phase, and the effective unit-cell are normalized by a characteristic modulus E_c which is chosen to be the Young's modulus of inter-bundle matrix E_m. All stress components are normalized by a characteristic stress Σ_c which is chosen to be the matrix microcracking initiation stress σ_c.

The normalized material and geometry parameters for a representative chemical vapor infiltrated (CVI) ceramic matrix plain weave fabric composite considered for this study, are listed in Table 1a. In the above table, the hat (^) notation is used to denote the normalized non-dimensional value. The mesoscopic effective tow elastic properties computed by the hierarchical approach presented in the work by Kuhn and Charalambides (1998a) are listed in Table 1b. The effective inter-bundle matrix properties are also listed in Table 1b. The unit-cell volume fractions occupied by the mesoscopic phases computed from the surface functions of the matrix layer geometry model are listed in the third column of Table 1b. Effective elastic properties of the undamaged unit-cell were obtained from the semi-analytical approximate model presented in the work by Kuhn et al. (1999) and are listed in the last column of Table 1b.

The non-linear stress–strain curves of the system under consideration for different values of the saturation microcrack density ϵ_s are presented in

Table 1
Micro-structural, mesoscopic, and unit-cell properties characteristic of a CVI ceramic matrix plain weave fabric composite

Fiber	Fiber coating	Matrix	Bundle coating	Volume fractions	Geometry
(a) Microstructural input parameters					
$\widehat{E}_{\mathrm{f}} = 0.5$	$\widehat{E}_{\mathrm{fc}} = 0.125$	$\widehat{E}_{\mathrm{m}} = 1.0$	$\widehat{E}_{\mathrm{bc}} = 0.25$	$C_{\mathrm{f}} = 0.5$	$\hat{a} = 1.0$
$\nu_{\mathrm{f}} = 0.2$	$\nu_{\mathrm{fc}} = 0.25$	$\nu_{\mathrm{m}} = 0.3$	$\nu_{\mathrm{bc}} = 0.25$	$C_{\mathrm{fc}} = 0.05$	$\hat{b} = 0.1$
				$C_{\mathrm{bm}} = 0.1$	$\hat{g} = 0.15$
				$C_{\mathrm{bp}} = 0.15$	$\hat{h} = 0.2$
				$C_{\mathrm{bc}} = 0.20$	$\hat{l} = 1.0$
				$C_{\mathrm{m}} = 1.0$	$\hat{t} = 0.03$
				$C_{\mathrm{mp}} = 0.0$	
(b) Meso- and macro-scopic output					
Effective tow	Effective matrix	Overall volume fractions	Undamage unit-cell		
$\widehat{E}_{11} = 0.346$	$\widehat{E}_{\hat{\mathbf{m}}} = 1.0$	$V_{\mathrm{fill}} = 0.272$	$\widehat{E}_x = 0.413$		
$\widehat{E}^{\ell}_{22} = 0.285$	$\widehat{G}_{\hat{\mathbf{m}}} = 0.385$	$V_{\mathrm{warp}} = 0.272$	$\widehat{E}_y = 0.413$		
$\widehat{G}_{12} = 0.119$	$\nu_{\hat{\mathbf{m}}} = 0.3$	$V_{\mathrm{matrix}} = 0.251$	$\nu_{xy} = 0.261$		
$\widehat{G}^{\ell}_{23} = 0.115$		$V_{\mathrm{void}} = 0.204$	$\nu_{yx} = 0.261$		
$\nu_{12} = 0.219$			$\widehat{G}_{xy} = 0.159$		
$\nu^{\ell}_{23} = 0.234$					

The listed properties were obtained using the hierarchical micro-mechanics model developed by Kuhn and Charalambides (1998a,b).

Fig. 4. In each plot, the normalized unit-cell stress $\hat{\sigma}^{\infty}$ is plotted against the normalized unit-cell strain $\hat{\varepsilon}^{\infty}$ for the indicated saturation microcrack density ϵ_{s} with $\lambda\sigma_{\mathrm{c}} = 1.0\mathrm{e}{+4}$. Note that the supercritical microcracking law requires that the microcracking rate λ is equal to infinity. In these simulations, a sufficiently large value equal to 1.0e+4, was used for the microcracking rate.

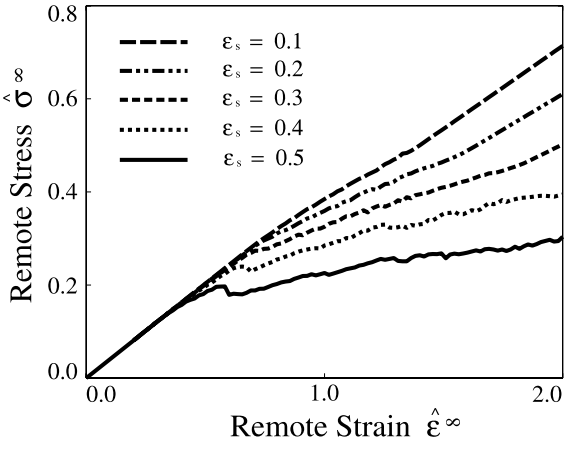

Fig. 4. Simulated non-linear stress–strain curves of the unit-cell with microstructure parameters listed in Table 1 for different values of ϵ_{s} and $\lambda\sigma_{\mathrm{c}} = 1.0\mathrm{e}{+4}$.

For each non-linear curve, a total of 100 strain increments were applied to achieve the final remotely applied unit-cell strain of $\hat{\varepsilon}^{\infty} = 2.0$. The reported curves were obtained using a 30×30 grid of integration stations within each domain element while also using a total of 3 integration stations within each mesoscopic phase in the z-direction. Initially the strain was increased by $\Delta\hat{\varepsilon}^{\infty} = 0.2$ from zero aiming at reducing unnecessary computations in the linear region without affecting the results. Subsequently, the remaining strain was applied in increments of $\Delta\hat{\varepsilon}^{\infty} = (2.0 - 0.2)/99$. The damage initiation occurred at the same point where $\hat{\varepsilon}^{\infty} = 0.29$ and $\hat{\sigma}^{\infty} = 0.13$ for every saturation microcrack density ϵ_{s}. Note that the damage initiation under subcritical conditions also occurred at $\hat{\varepsilon}^{\infty} = 0.29$ and $\hat{\sigma}^{\infty} = 0.13$ as reported in the work by Kuhn et al. (2000). On the other hand, Aubard et al. (1994) reported that the matrix cracking was observed to initiate approximately at $\hat{\varepsilon}^{\infty} = 0.3$ and $\hat{\sigma}^{\infty} = 0.2$, respectively. These values are of the same order as those predicted by the model. The difference in stress is likely due to the slight difference between the two systems, which is addressed by Kuhn et al. (2000).

3.1. Non-linear stress–strain curves

Some level of non-linear response is apparent in each of the plots presented in Fig. 4. For $\epsilon_s = 0.1$, there is a brief non-linear response, followed by a clear resumption of linearity, as also observed in the curves for $\epsilon_s = 0.2$ and $\epsilon_s = 0.3$. The sequence of linear, non-linear and again, linear response indicates that at these relatively low values of saturation microcrack density level, the microcrack density at every point in the woven unit-cell becomes saturated within the range of applied strain. It is worthwhile to note that this pattern is consistent with reference (Aubard et al., 1994), where three loading stages (linear, non-linear, and linear) were identified by monitoring acoustic emissions. As a result, the stress–strain curves reported by Aubard et al. (1994) appear to be highly consistent with the curves simulated herein. At higher levels of saturation density ($\epsilon_s = 0.4$ and 0.5), there is no apparent resumption of linearity within the selected range of applied strain. Instead, after the onset of microcracking damage, the curves are shown to exhibit local irregularities reminiscent of experimental data behaviors. This may be a direct consequence of the abrupt and rather unstable nature of the supercritical microcracking mechanism.

Carefully comparing the curves presented herein (see Fig. 4) with their subcritical counterparts reported by Kuhn et al. (2000), it is observed that the subcritical curves always exhibit higher stresses than those of the supercritical counterparts at the same level of applied strain. Under the subcritical microcracking condition, the microcrack density grows linearly up to its saturation level. Thus, even though the material is damaged, it still can sustain appreciable load until it is fully damaged. The supercritical microcracking condition, on the other hand, can only be associated with two distinct states of damage: undamaged or fully damaged states. As a result, at the same level of loading, the supercritical microcracking model exhibits lower load-carrying capacity than its subcritical counterpart as discussed above.

Experimental non-linear stress–strain curves are presented with simulated ones in Fig. 5. The experimental curves were obtained from tensile tests

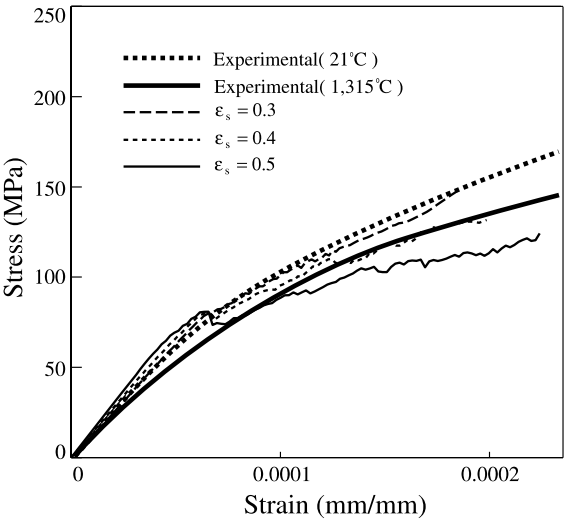

Fig. 5. Experimented stress–strain curves obtained by Williams International and CCI Inc. (Patterson, 1999) using a DuPont Lanxide SiC/SiC plain weave composite, are compared to supercritical microcracking stress–strain curves obtained for three different saturation densities, i.e. $\epsilon_s = 0.3$, 0.4 and 0.5 and $\lambda\sigma_c = 1.0e{+}4$.

of plain weave composites (DuPont Lanxide SiC/SiC) (Patterson, 1999). As presented in the figure, the simulated non-linear stress–strain curves are shown to exhibit a behavior similar to that of the experimental curves. Note that the CVI ceramic composite simulated in this study is comprised of Nicalon fibers and SiC matrix, while the details of the composite micro-structure were not identified.

The comparison to experiments presented in the paper is limited to the response of a SiC/SiC system. For this system, one can argue that thermal stresses play little if any role since the matrix and fiber constituents do not exhibit significant thermal expansion mismatches. It is in light of the above argument that the comparisons to experiments presented in Fig. 5 are made. The mechanical response of SiC/SiC woven composites is complex and intricately related to the material and geometrical complexity of the microstructure. The characterization of mechanical behavior of such complex systems requires experimental studies complemented by robust hierarchical modeling capable of preserving the integrity of the microstructure. The research presented in this paper

reflects a small step in an integrated effort to develop robust hierarchical models needed for the characterization of such complex systems. In that light, model predictions are compared to existing experiments as a means of establishing an overall envelope of material behavior and model prediction capabilities. The model comparison to experiments presented in Fig. 5 may suggest that the global non-linear composite response may, to a large extent, be attributed to the presence of non-linear matrix dominating damage processes captured by the super-critical micro-mechanics model put forth herein. However, the reader should remain critical on whether the current model fully captures the totality of non-linear processes that may concurrently activate during loading in such complex systems. Conclusive answers to the above question should be the outcome of further fundamental studies that bring together the certainty of experiments and the broadness of phenomenological modeling. As such, the research presented in this article does not reflect the end, but rather, it should signify the beginning of a broad modeling effort that ultimately is needed in helping the community of researchers and field engineers understand and thus make better use of this promising new class of material systems.

3.2. Effective property degradation

In Fig. 6, the non-linear stress–strain curves are plotted along with the respective effective elastic properties of the damaged unit-cell, for five different saturation microcrack densities. The effective properties presented in Fig. 6 represent the linear response of the damaged unit-cell at each level of loading. The methodology employed to calculate the effective properties of the unit-cell is presented in great detail in the work by Kuhn and Charalambides (1998a).

As shown in Fig. 6, in all cases presented, the properties remain constant up to the elastic limit at which the effective elastic properties start degrading. The property degradation becomes more pronounced with the higher microcrack density saturation level ϵ_s in accordance with the fact that the higher levels of ϵ_s represent the higher concentration of microcracks and thus lower load-bearing capacity at the associated damaged points. In systems with low microcracking capacity, in other words, low levels of ϵ_s, the in-plane effective elastic moduli $\widehat{E}_x$ and $\widehat{E}_y$ are shown to experience a brief differential degradation in the interval of $\hat{\epsilon}^{\infty}$ equal to 0.7–1.35. In the above loading regime, the in-plane modulus $\widehat{E}_x$ is shown to degrade more than the transverse modulus $\widehat{E}_y$. As a result of the locally isotropic microcracking law used in these simulations, for the cases of $\epsilon_s = 0.1$, 0.2, macroscopic damage-induced orthotropies persists only for a brief loading period which depends on ϵ_s as shown in Fig. 6. However, the results obtained for higher saturation densities indicate that, during loading, the evolution of microcracking degrades the effective modulus in the direction of loading at significantly higher rate compared to its orthogonal counterpart as shown in the plots for $\epsilon_s = 0.4$ and $\epsilon_s = 0.5$. Consistent with the stress–strain curves for $\epsilon_s = 0.4$ and $\epsilon_s = 0.5$ showing locally irregular behavior, the effective properties for the same cases exhibit similar tendencies (see Fig. 6).

When compared to the subcritical case results presented in the work by Kuhn et al. (2000), the supercritical results are observed to exhibit a moderately higher effective property degradation rate at the same load level. This confirms the relatively lower load-bearing capacity of a supercritical microcracking material (compared to its subcritical counterpart).

3.3. Volumetric matrix damage estimation

In this section, we report on the evolution of matrix damage-induced by the applied loads by monitoring the total volume of damaged matrix as a function of the applied strain. These results are presented in Fig. 7. As shown in the above figure, $V_{\mathrm{im}}^{\mathrm{d}}$ denotes the volume of damaged inter-bundle matrix, whereas $V_{\mathrm{fm}}^{\mathrm{d}}$ and $V_{\mathrm{wm}}^{\mathrm{d}}$ denote the volume of damaged matrix material within the fill and warp tows, respectively. Thus, the total volume of damaged matrix material is $V_{\mathrm{m}}^{\mathrm{d}} = V_{\mathrm{im}}^{\mathrm{d}} + V_{\mathrm{fm}}^{\mathrm{d}} + V_{\mathrm{wm}}^{\mathrm{d}}$. After upgrading the damage at each loading step, the damaged matrix volume is computed through a numerical volume integration of the data collected at each integration point of the three-dimensional integration grid (see Fig. 3).

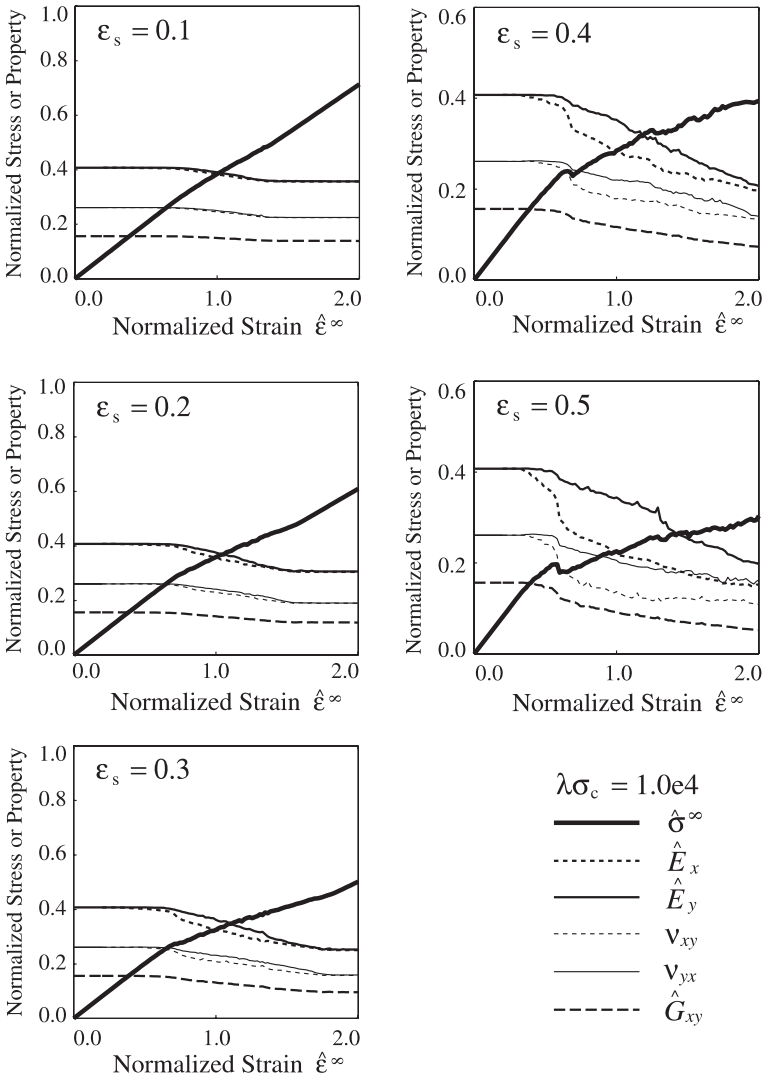

Fig. 6. Non-linear response and effective properties of the damaged unit-cell versus remote strain for $\lambda\sigma_c = 1.0e+4$.

Normalized volumetric matrix damages are presented in Fig. 7 as a function of the applied loading. Each plot contains five curves associated with five different saturation densities ϵ_s. In Fig. 7a, all curves intersect the remotely applied normalized strain axis $\hat{\varepsilon}^{\infty}$ at the same point, representing the critical strain at which the matrix microcracking initiates in the inter-bundle matrix phase. On the other hand, in Fig. 7b and c, the matrix damage initiations of the fill and warp tows are shown to be different for each saturation density level. In both phases, the matrix microcracking initiates earlier in the system with higher microcracking density saturation level. Closer observation of the above results reveals that in an overall sense, matrix microcracking first initiates in the inter-bundle matrix phase. The critical matrix damage initiation strain $(\hat{\epsilon}_x^{\infty})_c$ in each phase for five different saturation levels are listed in Table 2. As shown, the matrix damage initiation of the inter-bundle matrix phase is independent of the saturation level ϵ_s, while those of the bundle

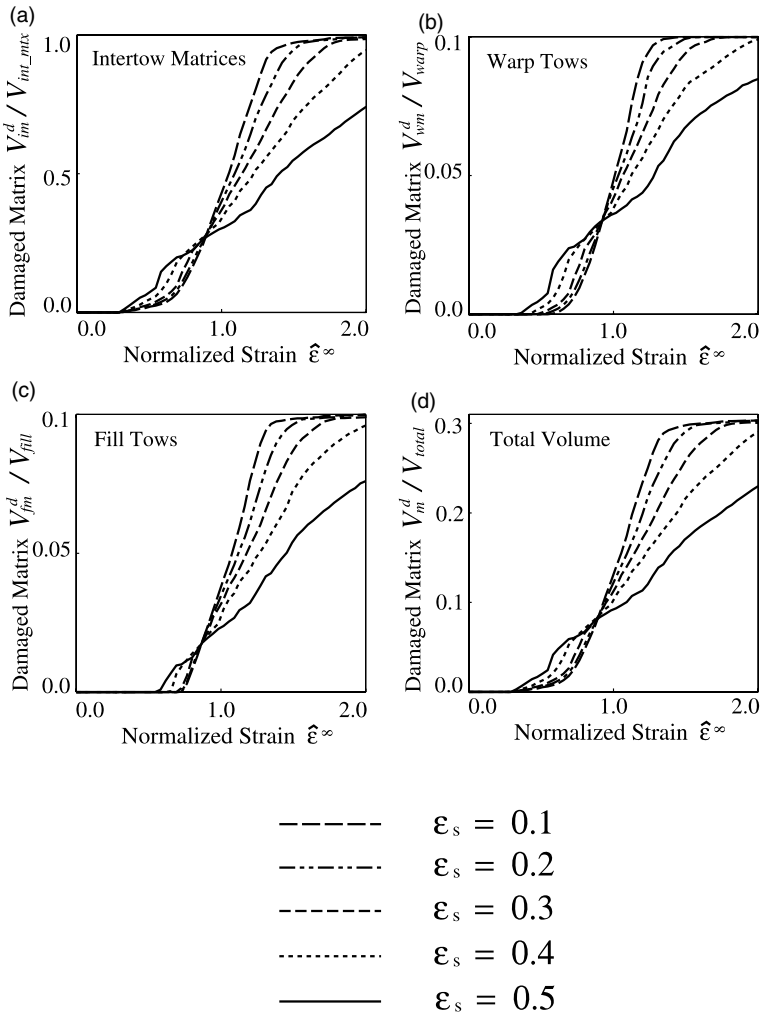

Fig. 7. The volume fraction of damaged matrix versus remote strain calculated for (a) the intertow matrix, (b) the warp tows, (c) the fill tows, and (d) the entire unit-cell. The reported results were obtained for five saturation microcrack density levels.

Table 2
The matrix damage initiation loads $(\hat{\varepsilon}_x^\infty)_c$ in each mesoscopic phase for five different saturation levels

Phase	$(\hat{\epsilon}_x^\infty)_c$				
	$\epsilon_s = 0.1$	$\epsilon_s = 0.2$	$\epsilon_s = 0.3$	$\epsilon_s = 0.4$	$\epsilon_s = 0.5$
Inter-bundle matrices	0.2909	0.2909	0.2909	0.2909	0.2909
Warp tows	0.5818	0.5454	0.4727	0.4363	0.3636
Fill tows	0.7272	0.7272	0.7272	0.6545	0.5818

matrices are clearly dependent on ϵ_s. In addition to the above, the results reported in Fig. 7 suggest that the damage spreads faster in systems characterized by the lower saturation microcracking densities. This is evident in all plots in Fig. 7, where both the inter-bundle matrix and bundle

matrix are shown to be fully damaged for systems with the relatively lower saturation levels ($\epsilon_s = 0.1$, 0.2, 0.3) while, other systems with the higher saturation levels ($\epsilon_s = 0.4$, 0.5) remain only partially damaged. This observation makes intuitive sense, since systems with the higher saturation level ϵ_s lose more load-bearing capacity consistent with the higher effective property degradation rate in the vicinity of the existing damaged zone.

In Fig. 8, the in-plane effective elastic properties reported in Fig. 6 are plotted against the normalized volumetric matrix damage V_m^d/V_{total} for the entire system. As expected, each property degrades with increasing volumetric matrix damage V_m^d/V_{total}. The results reported in Figs. 7 and 8 make possible, for the first time, the development of empirical matrix damage-induced degradation laws for the effective moduli of a microcracking woven unit-cell. As the first step of developing the empirical laws mentioned above, it is found that all the curves reported in Fig. 7d can be approximated by using the following empirical formula:

$$\frac{V_m^d}{V_{total}} = 0.154[\mathrm{erf}(A(\hat{\varepsilon}_x^{\infty} - B) + C)] \tag{5}$$

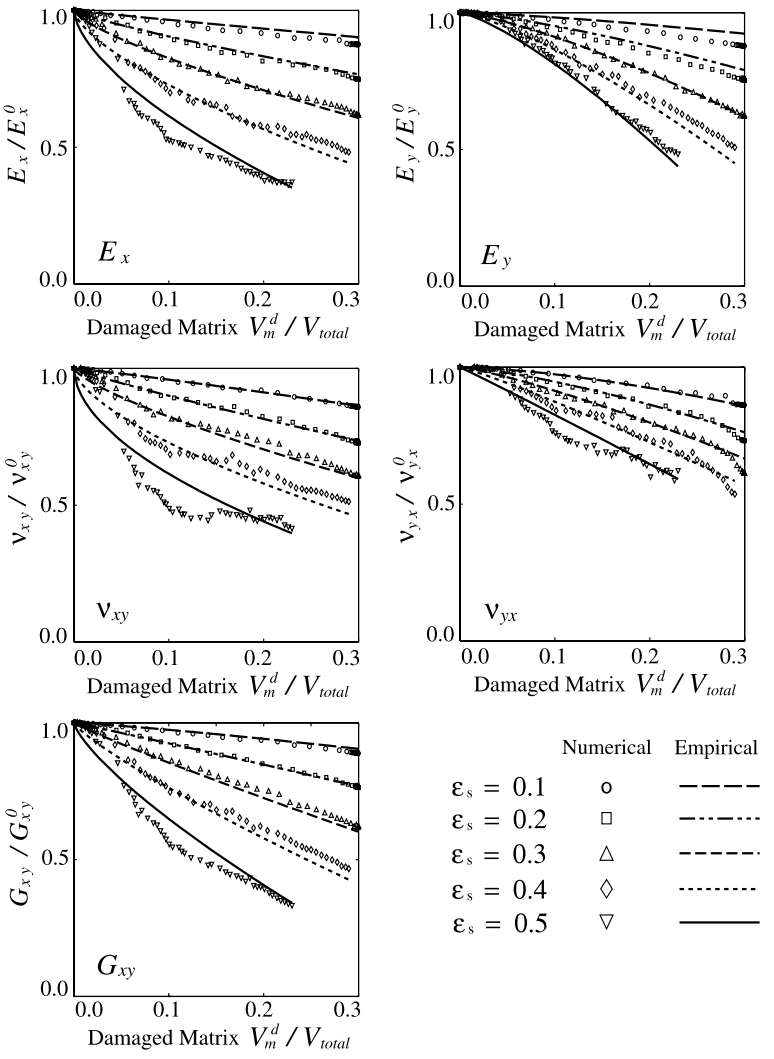

Fig. 8. Effective property degradation rate plotted against the overall volume fraction of damaged matrix for different values of ϵ_s.

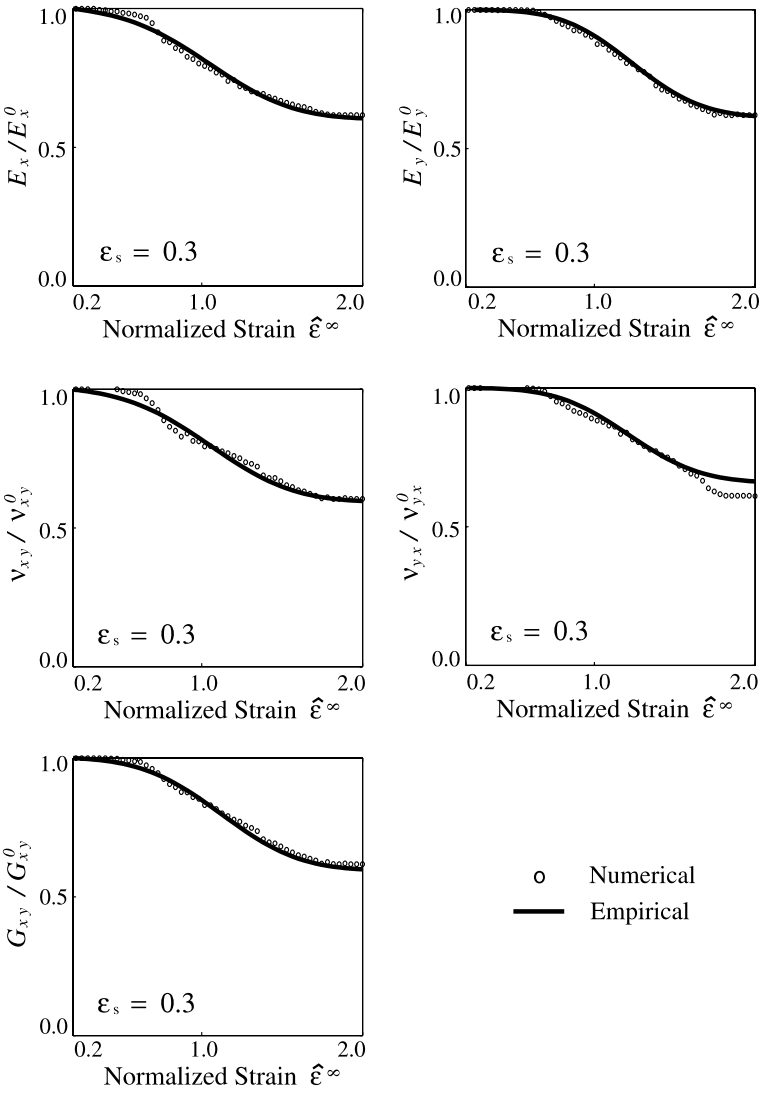

Fig. 9. Elastic property degradation profiles obtained for $\epsilon_s = 0.3$. The solid lines represent the empirical law (see Eqs. (7)–(11)) predictions while the open symbols represent numerical predictions obtained using the supercritical microcracking model.

where

$$\begin{cases} \operatorname{erf}(x) = \frac{2}{\sqrt{\pi}} \int_0^x \mathrm{e}^{-t^2}\,\mathrm{d}t \\ A = -4.74\epsilon_s + 3.3 \\ B = -2.62(\epsilon_s - 0.32)^2 + 1.15 \\ C = \left(\mathrm{e}^{1-\epsilon_s^{6.9}}\right)^{49.2} \end{cases} \tag{6}$$

The function $\operatorname{erf}(x)$ appearing in Eqs. (5) and (6) above is known as the error function, which is commonly used in the field of Statistics. Each of the in-plane moduli follows a universal degradation law for all the saturation density levels as follows:

$$\widehat{E}_x = \widehat{E}_x^0 \left[1 - 3.3\epsilon_s^{1.03} \left(\frac{V_m^d}{V_{total}} \right)^{2.0 - 1.55\epsilon_s^{0.17}} \right] \tag{7}$$

$$\widehat{E}_y = \widehat{E}_y^0 \left[1 - 8.8\epsilon_s^{1.33} \left(\frac{V_m^d}{V_{total}} \right)^{2.0 - 0.75\epsilon_s^{0.03}} \right] \tag{8}$$

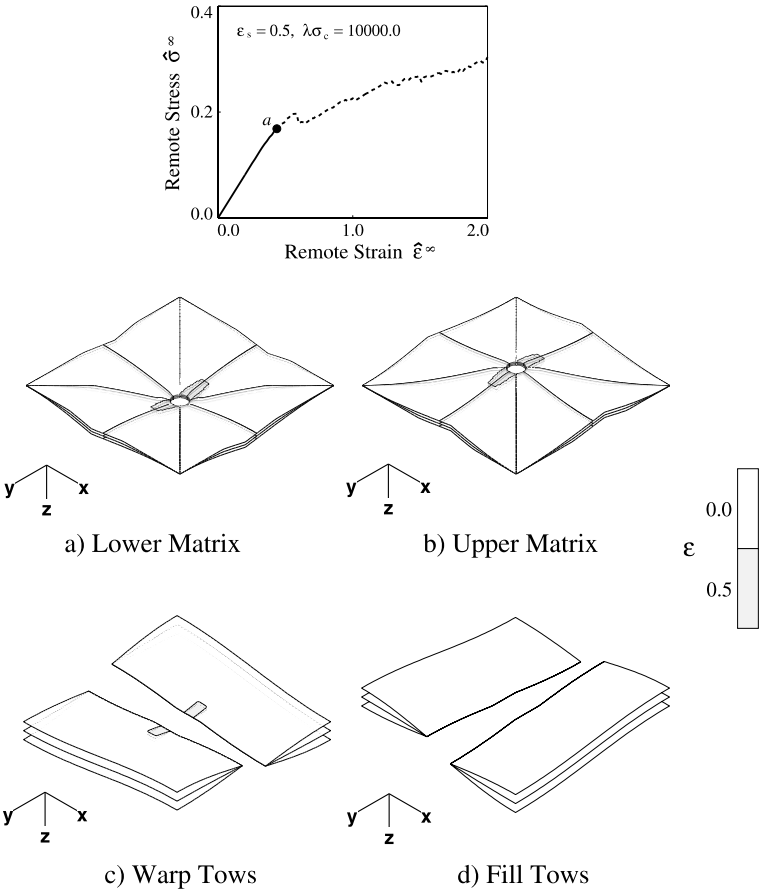

Fig. 10. Fringes of the microcrack density ϵ after damage initiation, corresponding to loading point a. The remote uniaxial strain loading is applied in the x-direction.

$$\hat{\nu}_{xy} = \hat{\nu}^0_{xy}\left[1 - 2.0\epsilon_s^{0.59}\left(\frac{V_m^d}{V_{total}}\right)^{2.0-1.8\epsilon_s^{0.3}}\right] \tag{9}$$

$$\hat{\nu}_{yx} = \hat{\nu}^0_{yx}\left[1 - 2.5\epsilon_s^{0.44}\left(\frac{V_m^d}{V_{total}}\right)^{2.0-1.35\epsilon_s^{0.47}}\right] \tag{10}$$

$$\widehat{G}_{xy} = \widehat{G}^0_{xy}\left[1 - 4.0\epsilon_s^{1.0}\left(\frac{V_m^d}{V_{total}}\right)^{2.0-1.5\epsilon_s^{0.27}}\right] \tag{11}$$

Thus, when combining Eq. (5) and Eqs. (7)–(11), the in-plane effective moduli can be expressed in terms of the remotely applied strain $\hat{\varepsilon}^{\infty}$. The in-plane moduli predicted using the above empirical laws for the case of $\epsilon_s = 0.3$ are presented in Fig. 9 along with their numerical counterparts. As shown, the empirical formulas capture the degraded effective in-plane properties with great deal of accuracy. It is expected that the empirical moduli degradation formulas presented in this work will lay the foundation for the development of sound and sensible phenomenological continuum models capable of accurately modeling the damage-induced non-linear response of woven CMCs. As such, complementary studies are now being conducted aiming at establishing the requisite moduli degradation laws governing woven CMCs subjected to a general in-plane loading.

3.4. Damage zones

While the resulting effects of damage evolution such as the non-linear response of the system, the degradation of the in-plane effective properties, and the evolution of the volumetric matrix damage were extensively addressed above, there also exists the need to visualize the formation and evolution of microcracking damage within the unit-cell with increasing applied strains. Three layered 2-D meshes coinciding with the Gauss integration stations where the matrix microcrack densities are actually evaluated, are introduced at each mesoscopic phase for the purpose of displaying fringes of the matrix microcrack density. The unit-cell fringes at four points carefully selected along the stress–strain curve for $\epsilon_s = 0.5$ and $\lambda\sigma_c = 1.0\text{e+}4$ are shown in Figs. 10–13.

The above sequence of microcrack density fringes offers a great insight on the progression of damage in the matrix material of the unit-cell. For example, the damage zones shown in Fig. 10 were obtained at a loading state marked by point *a* on the stress–strain curve displayed on the top of the figure. At this point, the inter-bundle matrix material has sustained a limited amount of damage, while also showing that damage has, at the same time, initiated in the matrix material in the warp tows. No damage is shown in the fill tows at this loading stage.

At the point immediately following the "knee" region of the stress–strain curve (point *b*), the

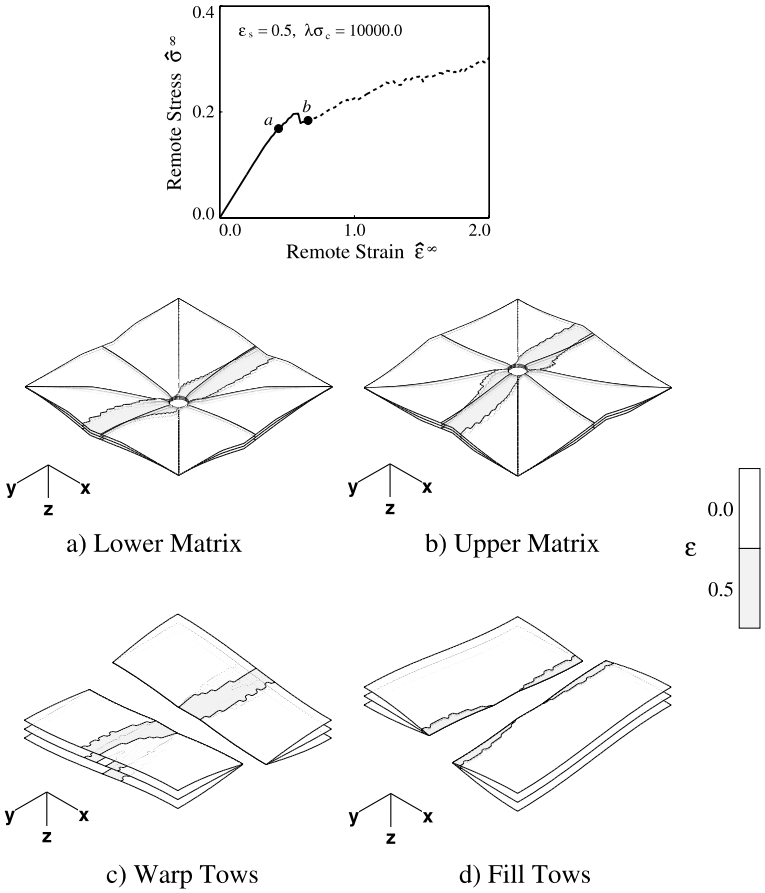

Fig. 11. Fringes of the microcrack density ϵ after the knee behavior, corresponding to loading point *b*. The *x*-direction is the loading direction.

fringes presented in Fig. 11 illustrate that the inter-bundle matrix damage has propagated outward in the direction perpendicular to the applied loading, forming a narrow damage band across the woven unit-cell which resembles a mode-I matrix crack. At this stage of loading, there is evidence of damage progression in the matrix material of the warp tows as well as the fill tows. It is quite obvious that the damage in the warp tows and the fill tows can be associated with cracking phenomena such as bundle matrix cracking and transverse bundle matrix cracking, respectively.

In Fig. 12 corresponding to point *c* of the stress–strain curve, the narrow damaged band in the inter-bundle observed in Fig. 11 has become broader. As a result, the matrix material sustains significantly reduced load and most of the load is transferred through the fiber reinforcements and the warp tows. This simulates the evolution of a well-formed matrix crack in the fill tows bridged by the tow fiber reinforcements.

The damage zones of Fig. 13 show that the matrix material in the warp and fill tows has sustained appreciable damage at this stage of loading (point *d*). As shown, only a small portion of the unit-cell domain remains damage-free. It is possible that other micro-failure events such as bundle delamination, fiber failure and pull-out, which are not accounted for in this study, may in fact be active at this level of loading.

While recognizing the limitation of this model, the damage zones reported in Figs. 10–13 do yield

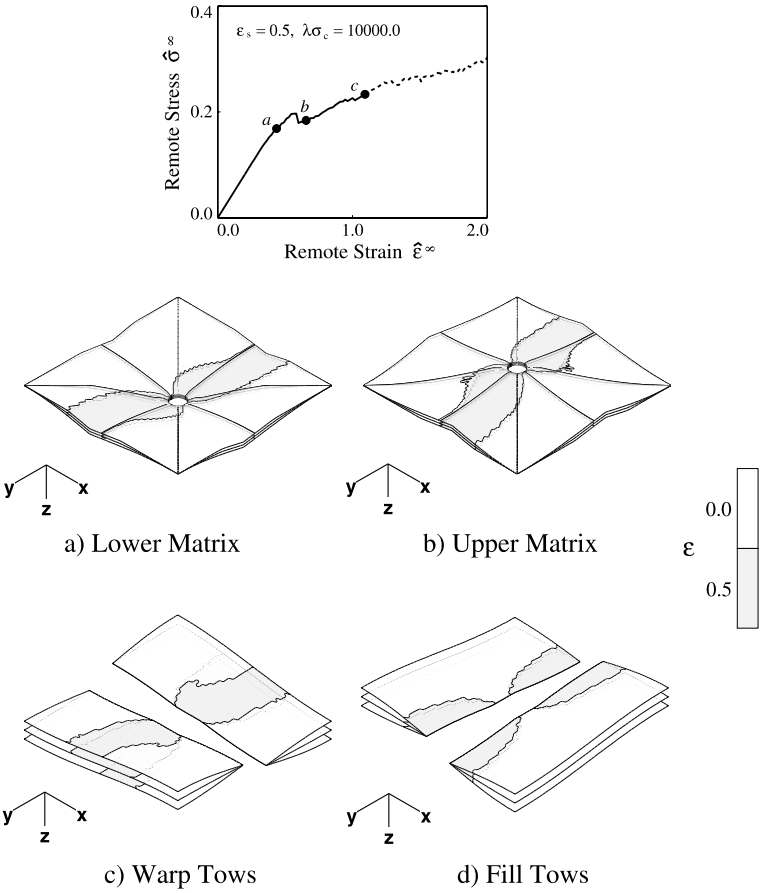

Fig. 12. Fringes of the microcrack density ϵ, associated with loading point *c*, induced by uni-directional remote loading in the *x*-direction.

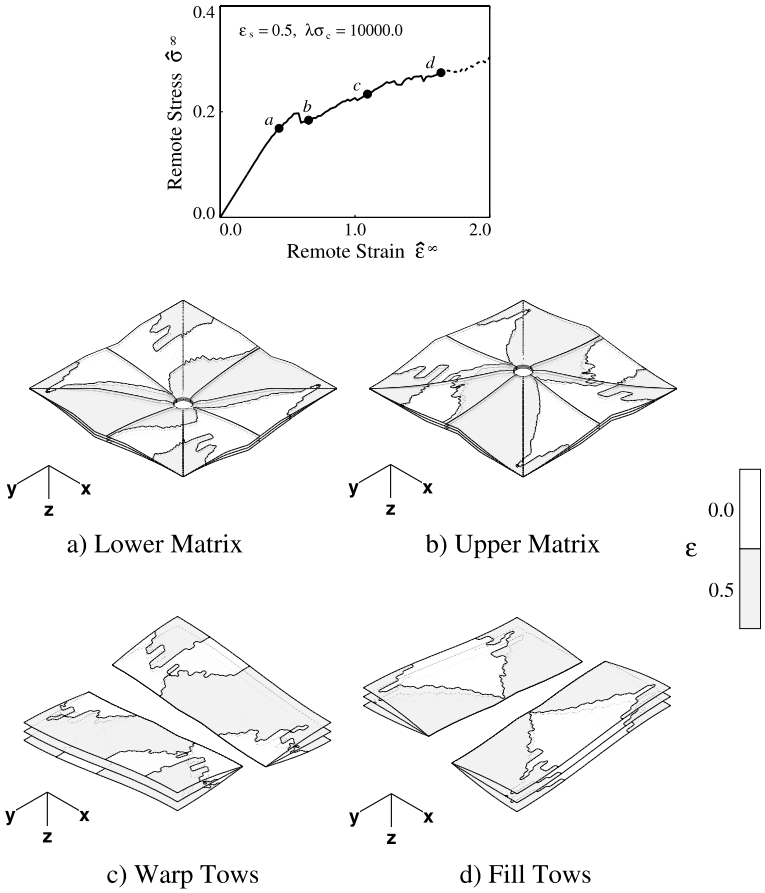

Fig. 13. Fringes of the microcrack density ϵ, associated with loading point d, due to loading in the x-direction.

appreciable insights regarding the evolution of supercritical damage zones in woven CMCs. For example, the above results demonstrate that matrix damage should be expected to evolve in directions perpendicular to the direction of applied loading. While the inter-bundle matrix phase appears to be the most susceptible to microcracking damage, the bundle matrix in the warp tows which are aligned with the direction of loading in this study, also experience localized mode-I cracking similar to that predicted for the inter-bundle matrix phase. On the other hand, the fill tows which are in the direction perpendicular to the applied loading exhibit damage characteristics consistent with transverse matrix cracking parallel to the fiber reinforcements.

4. Conclusions

This work represents a continuous effort to model the non-linear response of ceramic matrix plain weave composites. The supercritical matrix microcracking model capable of accounting for the abrupt loss of material stiffness due to microcracking, developed in this study was used to simulate the damage-induced non-linear response of ceramic matrix woven systems.

Analytical and hierarchical micro-mechanics models capable of capturing the intricate three-dimensional micro-stress fields due to a general in-plane loading were embedded within the non-linear iterative scheme used to update the load induced micro-damage. A wide range of non-linear

stress–strain curves under remote tension were obtained. The irregularities of the curves are attributed to the abrupt loss of material stiffness under the adopted supercritical microcracking condition. Matrix cracking initiation was found to be independent of the saturation microcracking density ϵ_s. It was shown that matrix microcracking first initiates in the inter-bundle matrix in the high stress concentration region around the large matrix void. The model predictions were found to be in good agreement with experimentally obtained stress–strain curves.

Extensive parametric study results were used to develop empirical strain-induced damage accumulation and moduli degradation laws. The latter findings can assist the development of sensible phenomenological continuum models capable of modeling the damage evolution and non-linear response of ceramic matrix woven composites.

Acknowledgements

This work was partially supported by the National Science Foundation, Grant no. CMS94-96209 and by Technology Assessment and Transfer and Ceramic Composites Inc. of Anapolis, MD.

References

Aubard, X., Lamon, J., Allix, O., 1994. Model of the nonlinear mechanical behavior of 2D SiC–SiC chemical vapor infiltration composites. J. Am. Ceram. Soc. 77 (8), 2118–2126.

Bassani, J.L., 1991. Linear densification and microcracking in sintering compacts. Mech. Mater. 12, 119–130.

Budiansky, B., O'Connell, R.J., 1976. Elastic moduli of a cracked solid. Int. J. Solids Struct. 12, 81–97.

Charalambides, P.G., McMeeking, R.M., 1987. Finite element method simulation of crack propagation in a brittle microcracking solid. Mech. Mater. 6, 71–87.

Charalambides, P.G., McMeeking, R.M., 1988. Near-tip mechanics of stress-induced microcracking in brittle materials. J. Am. Ceram. Soc. 71 (6), 465–472.

Fu, Y., Evans, A.G., 1985. Some Effects of microcracks on the mechanical properties of brittle solids-I. Stress, strain relations. Acta Metall. 33 (8), 1515–1523.

Giannakopoulos, A.E., 1989. Fracture Mechanics of Monolithic Ceramic Materials under Smallscale Microcracking Conditions. Ph.D. Thesis, Brown University.

Giannakopoulos, A.E., 1990. Dynamic damage in certain monolithic ceramic materials. J. Appl. Mech. 58, 639–643.

Hashin, Z., 1983. Analysis of composite materials—a survey. J. Appl. Mech. 50, 481–505.

Hashin, Z., 1990. Analysis of damage in composite materials. In: Boehler, J.P. (Ed.), Proc. IUTAM/ICM Symposium on Yielding, Damage and Failure of Anisotropic Solids. Mechanical Engineering Publishers, pp. 3–32.

Hashin, Z., 1991. Micromechanics aspects of damage in composite materials. In: Cradon, A.H. et al. (Eds.), Durability of Composite Material Systems. Elsevier Applied Science, pp. 27–45.

Hashin, Z., 1995. Cracked laminates with imperfect interlamina interface. In: Pyrz, R. (Ed.), Microstructure-Property Interactions in Composite Materials. Kluwer Academic Publishers, pp. 113–128.

Hoagland, R.G., Embury, J.D., 1980. A treatment of inelastic deformation around a crack tip due to microcracking. J. Am. Ceram. Soc. 63 (7–8), 404–410.

Hoagland, R.G., Embury, J.D., Green, D.J., 1976. On the density of microcracks formed during the fracture of ceramics. Scr. Metall. 9, 907–909.

Hoenig, A., 1979. Elastic moduli of a non-randomly cracked body. Int. J. Solids Struct. 15, 137.

Hoenig, A., 1982. Near-tip behavior of a crack in a plane anisotropic elastic body. Engng. Fract. Mech. 16, 393.

Horii, H., Nemat-Nasser, S., 1983a. Estimates of stress intensity factors for interacting cracks. In: Yuceoglu, U. et al. (Eds.), Advances in Aerospace Structures, Materials and Dynamics. ASME, New York, p. 111.

Horii, H., Nemat-Nasser, S., 1983b. Overall moduli of solids with microcracks: load-induced anisotropy. J. Mech. Phys. Solids 31, 155.

Ishikawa, T., Chou, T., 1982a. Elastic behavior of woven hybrid composites. J. Compos. Mater. 16, 2–9.

Ishikawa, T., Chou, T., 1982b. Stiffness and strength behaviour of woven fabric composites. J. Mater. Sci. 17, 3211–3220.

Ishikawa, T., Chou, T., 1983a. In-plane thermal expansion and thermal bending coefficients of fabric composites. J. Compos. Mater. 17, 92–104.

Ishikawa, T., Chou, T., 1983b. One-dimensional micromechanical analysis of woven fabric composites. Am. Inst. Aeronautics Astronautics J. 21 (12), 1714–1721.

Krajcinovic, D., 1985. Continuous damage mechanics revisited: basic concepts and definitions. J. Appl. Mech. 52, 829–834.

Krajcinovic, D., Fonseka, G.U., 1981. The continuous damage theory of brittle materials: Parts I and II. J. Appl. Mech. 48, 809–824.

Kuhn, J.L., Charalambides, P.G., 1998a. Elastic response of porous matrix plain weave fabric composites: Part I—modeling. J. Compos. Mater. 32 (16), 1426–1471.

Kuhn, J.L., Charalambides, P.G., 1998b. Elastic response of porous matrix plain weave fabric composites: Part II—results. J. Compos. Mater. 32 (16), 1472–1507.

Kuhn, J.L., Charalambides, P.G., 1999. Modeling of plain weave fabric composite geometry. J. Compos. Mater. 33 (3), 187–220.

Kuhn, J.L., Haan, S.I., Charalambides, P.G., 1999. A semi-analytical method for the calculation of the elastic micro-fields in plain weave fabric composites subjected to in-plane loading. J. Compos. Mater. 33 (3), 221–266.

Kuhn, J.L., Haan, S.I., Charalambides, P.G., 2000. Stress-induced matrix microcracking in brittle matrix plain weave fabric composites under uniaxial tension. J. Compos. Mater. 34 (19), 1640–1664.

Lambropoulos, J.C., 1988. Shear shape and orientation effects in transformation toughening. Int. J. Solids Struct. 22 (10), 1083–1106.

Ortiz, M., Giannakopoulos, A.E., 1989. Maximal crack tip shielding by microcracking. J. Appl. Mech. 56, 279–283.

Patterson, M.C.L., 1999. Ceramic Composites, Inc., Private communication.

Voyiadjis, G.Z., 1995a. Anisotropic damage of fiber reinforced MMC using an overall damage analysis. J. Engng. Mech. 121 (11), 1209–1217.

Voyiadjis, G.Z., 1995b. Local and interfacial damage analysis of matal matrix composites. Int. J. Engng. Sci. 33 (11), 1595–1621.

Wang, H., Singh, R.N., 1994. Thermal shock behavior of ceramics and ceramic composites. Int. Mater. Rev. 39 (6), 228–244.

Whitcomb, J.D., 1991. Three-dimensional stress analysis of plain weave composites. In: Composite Materials: Fatigue and Fracture. In: ASTM STP 1110, vol. 3. American Society for Testing and Materials, Philadelphia, pp. 417–438.